



# A metal-organic framework-derived bifunctional catalyst for hybrid sodium-air batteries

Yuqi Wu<sup>a</sup>, Xuechao Qiu<sup>a</sup>, Feng Liang<sup>a,b,\*</sup>, Qingkai Zhang<sup>a</sup>, Alicia Koo<sup>c</sup>, Yongnian Dai<sup>a</sup>, Yong Lei<sup>d</sup>, Xueliang Sun<sup>c</sup>

<sup>a</sup> Faculty of Metallurgical and Energy Engineering, Kunming University of Science and Technology, Kunming 650093, China

<sup>b</sup> State Key Laboratory of Complex Non-ferrous Metal Resources Clean Application, Kunming University of Science and Technology, Kunming 650093, China

<sup>c</sup> Department of Mechanical and Materials Engineering, University of Western Ontario, London, Ontario N6A 5B9, Canada

<sup>d</sup> Institute of Physics & IMN Macro Nanos (ZIK), Ilmenau University of Technology, Unterpörlitzer Strasse 38, Ilmenau 98693, Germany

## ARTICLE INFO

### Keywords:

Metal-organic framework  
Electrocatalyst  
Sodium-air batteries  
N-doped carbon nanotubes  
Confined Co nanoparticles

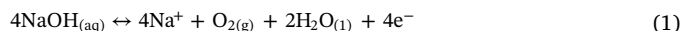
## ABSTRACT

Metal-organic framework (MOF)-derived carbon nanomaterials are investigated as promising non-noble metal-based oxygen electrocatalysts for metal-air batteries. Herein, metal-organic framework-derived N-doped carbon nanotubes (MOF-NCNTs) were first employed as electrocatalysts for hybrid sodium-air batteries (SABs), which exhibited higher electrocatalytic activity and stability for the oxygen reduction reaction (ORR) and oxygen evolution reaction (OER) compared to commercial Pt/C. The battery using MOF-NCNTs displayed the voltage gap of 0.30 V at a current density of 0.1 mA cm<sup>-2</sup>, which is the lowest among all the tested catalysts including commercial Pt/C (0.50 V), RuO<sub>2</sub> (0.50 V), Co-CNTs (0.67 V), NCNTs (0.77 V), MWNTs (0.90 V), and carbon paper (1.18 V). In addition, the average discharge plateau and round trip efficiency of the battery was 2.81 V and 87% during 35 cycles at a current density of 0.1 mA cm<sup>-2</sup>, respectively. The remarkable electrocatalytic activity is mainly ascribed to the synergistic effect between the N dopants and confined Co nanoparticles in the CNTs, the hollow structure of NCNTs, and the robust porous cage structure. The N dopants and confined Co nanoparticles in the CNTs induce more catalytic active sites and promote electron transfer for the ORR and OER. The hollow framework structure of NCNTs not only offer structural defect sites for O<sub>2</sub> adsorption, but also improves mass transport and electronic conductivity, resulting in enhanced catalytic activity. The robust porous cage structure contributes to the stability of the catalysts. The highly efficient and inexpensive metal-organic framework-derived NCNT is a promising bifunctional oxygen electrocatalyst for practical applications in hybrid SABs and other metal-air batteries.

## 1. Introduction

Over the past few years, considerable research has been devoted to developing rechargeable sodium-air batteries (SABs) due to its high theoretical specific capacity, high energy density, low cost, and low environmental impact [1–6]. Two categories of SABs, non-aqueous and aqueous/hybrid, are divided on the basis of electrolytes used in the system [2,7]. The electrochemical performance of non-aqueous SABs are limited by the insolubility of solid discharge products (e.g. Na<sub>2</sub>O and Na<sub>2</sub>O<sub>2</sub>) which hinder the long-term operation by clogging the air electrode [8–13]. Moreover, the battery system demands an auxiliary pure oxygen tank to supply oxygen and prevent impurities from entering the electrolytes [14,15]. In contrast, hybrid SABs can remove the impact of insoluble discharge products by employing an aqueous

electrolyte, such as NaOH or acidic catholyte composed of NaNO<sub>3</sub> and citric acid [2,5]. The NaOH electrolyte participates in the ORR and OER at the cathode as follows:



The discharge product is therefore the extremely water-soluble NaOH, thus improving the battery performance. Hybrid SABs exhibit a higher theoretical standard cell voltage of 3.11 V, a higher theoretical specific capacity of 838 mA h g<sup>-1</sup>, and a lower overpotential than non-aqueous SABs [1–13].

However, the ORR and OER at the cathode are sluggish, resulting in large overpotentials and poor cycling stability during the charge-discharge process [2,16]. The typical solution to this problem is to use an electrochemical catalyst to promote the ORR and/or OER [16–18]. For

\* Corresponding author at: Xuefu Road 253, Kunming City, Yunnan Province 650093, China.

E-mail address: [liangfeng@kmust.edu.cn](mailto:liangfeng@kmust.edu.cn) (F. Liang).

<https://doi.org/10.1016/j.apcatb.2018.09.063>

Received 29 May 2018; Received in revised form 14 September 2018; Accepted 19 September 2018

Available online 20 September 2018

0926-3373/© 2018 Elsevier B.V. All rights reserved.

instance, Liang et al. first proposed  $\text{Mn}_3\text{O}_4/\text{C}$  as an effective catalyst for hybrid SABs, which exhibits a discharge voltage of 2.60 V at a current density of  $1 \text{ mA}\cdot\text{cm}^{-2}$  [4]. Subsequently, dual-phase spinel  $\text{MnCo}_2\text{O}_4$  with nitrogen-doped reduced graphene oxide hybrids ( $\text{dp-MnCo}_2\text{O}_4/\text{N-rGO}$ ) were employed as electrocatalysts in hybrid SABs, which exhibited superior catalytic performance compared to commercial Pt/C [3]. Kim et al. reported that a Pt/C-coated carbon paper catalyst for hybrid SABs showed a high and stable discharge voltage of 2.85 V and a high voltage efficiency of 84.3% at a current density of  $0.025 \text{ mA}\cdot\text{cm}^{-2}$  [16]. However, the scarcity and high cost of Pt/C are major barriers for the large-scale application of the air electrodes [19]. Cheon et al. investigated the charge-discharge curve of hybrid SABs with different electrocatalyst-coated carbon papers and found that although graphitic nanoshell/mesoporous carbon nanohybrids (GNS/MC)-based batteries exhibit a low charge-discharge polarization of about 115 mV [20], the ORR activity is unsatisfactory. In addition, it is difficult to prepare this material on a large scale due to the complicated synthetic method. Abirami et al. applied porous cobalt manganese oxide (CMO) nanotubes as the cathode electrocatalyst in rechargeable aqueous SABs/seawater batteries, displaying good cycling performance and ORR activity [21], but the CMO catalyst showed a high charge voltage, resulting in a large voltage gap of 0.53 V at a current density of  $0.01 \text{ mA}\cdot\text{cm}^{-2}$ .

Metal-organic frameworks (MOFs) are a novel type of porous crystalline material that possess high specific surface area, controllable structure, tunable pore sizes, and customizable framework functionalities. The diversity of framework structures are a result of different types of covalent bonding which allow for a variety of MOF-derived nanocomposites [22–24]. Hence, MOFs are considered as alternative precursors for various types of nanocarbon composites [25,26]. Previous studies have demonstrated that the MOF-derived N, S-co-doped nanocarbon electrocatalyst exhibits high catalytic activity toward the ORR [27]. Yang et al. reported the first example of the synthesis of NCNTs using Zn-Fe-ZIFs nanospheres [28]. The robust network of aligned NCNTs not only improved mass transport, but also provided more available active sites, resulting in enhanced catalytic activity of electrocatalysts [11,29–31]. Subsequently, Xia et al. reported the synthesis of an N-doped carbon nanotube framework (NCNTFs) derived from ZIF-67, which exhibit remarkable electrocatalytic activity for ORR and OER compared to commercial Pt/C [32]. However, the mechanism of catalysis was not explained in depth and the use of MOF-derived carbon nanomaterial electrocatalysts for SABs have rarely been reported [21,24]. This opens up new possibilities for exploring other MOF-derived carbon nanomaterials as highly effective bifunctional electrocatalysts for SABs.

Herein, we report the enhanced electrochemical performance of hybrid SABs by using MOF-NCNTs as an active and stable bifunctional electrocatalyst for ORR and OER. The porous cage structure of MOF-NCNTs are obtained by a simple heat-treatment of polyhedral ZIF-67 particles, resulting in catalysts that exhibit excellent activity and durability compared with commercial Pt/C and  $\text{RuO}_2$  in hybrid SABs. These results reveal that the remarkable electrocatalytic properties of MOF-NCNTs can be ascribed to the synergistic effect between N dopants and confined Co nanoparticles in CNTs, the CNT structure, as well as the robust open porous framework structure.

## 2. Experimental

### 2.1. MOF-NCNT catalyst preparation

The MOF-NCNT materials were synthesized by the heat-treatment of purple ZIF-67 particles under a mixture of Ar and  $\text{H}_2$  atmosphere. The purple ZIF-67 precursor particles were obtained by a chemical coprecipitation method at room temperature [32]. 7.88 g 2-methylimidazole (Macklin, 98%) was first dissolved in a solvent mixture of 80 mL methanol and 80 mL ethanol to form a clear solution and 6.984 g Co  $(\text{NO}_3)_2\cdot 6\text{H}_2\text{O}$  (Macklin, 99%) was dissolved in a separate identical

solvent mixture to form a red solution. The two solutions were then mixed in a beaker, stirred for 60 s, and maintained at room temperature for 20 h to form a purple precipitate. The precipitate was then separated by centrifugation, washed with ethanol, and dried at  $80^\circ\text{C}$  for 10 h. Finally, the purple ZIF-67 particles were calcined to form the MOF-NCNTs by heating under Ar/ $\text{H}_2$  flow (9:1 in volume) at  $350^\circ\text{C}$  for 135 min with a ramp rate of  $2^\circ\text{C}\cdot\text{min}^{-1}$  then maintaining the temperature at  $700^\circ\text{C}$  for 315 min. The resulting as-prepared black powder was added to a 0.5 M  $\text{H}_2\text{SO}_4$  solution for 6 h. The products were obtained by centrifugation, washed with distilled water several times, and then dried at  $80^\circ\text{C}$ . For comparison, other products were synthesized according to a similar thermal treatment process at  $650^\circ\text{C}$  and  $750^\circ\text{C}$ .

### 2.2. MOF-NCNT catalyst characterizations

The morphology and microstructure of MOF-NCNTs were observed by field-emission scanning electron microscopy (FESEM; Hitachi, SU8010) at 3.0 kV, transmission electron microscopy (TEM; JEOL, JEM-2100) at 200 kV, and X-ray diffraction (XRD; Rigaku, D/max-TTR III) operated with Cu  $\text{K}\alpha$  X-ray source. The chemical bonding state and composition were analyzed by X-ray photoelectron spectroscopy (XPS; PHI, PHI5000) with a Mg  $\text{K}\alpha$  X-ray source at a scan rate of  $0.02^\circ\cdot\text{s}^{-1}$ . HAADF-STEM with energy-dispersive X-ray spectrometry (EDS) images was obtained using a FEI Titan G2 60–300 electron microscope with an accelerating voltage of 300 kV. Raman spectra were recorded using a LabRAM HR evolution spectroscopy system (Raman, HORIBA). The  $\text{N}_2$  sorption isotherms are collected using a Quadrasorb evo at liquid-nitrogen temperature.

### 2.3. Rotating-disk electrode (RDE) measurements

The catalytic activity of the MOF-NCNT electrocatalyst for ORR and OER was analyzed using a rotating disk electrode (RDE, HP-1 A, China) based on a three-electrode cell, where platinum foil and Ag/AgCl (3.0 M KCl) were used as the counter electrodes and reference electrode, respectively. All test results were converted to potentials versus RHE according to the following relationship:

$$E_{(\text{RHE})} = E_{(\text{Ag/AgCl})} + 0.0591 \times \text{pH} + 0.2046 \quad (2)$$

The ORR performance was measured in an  $\text{O}_2$ -saturated 0.1 M KOH solution at various rotation rates with a scan of  $10 \text{ mV}\cdot\text{s}^{-1}$ . RDE linear sweep voltammetry (LSV) for OER was performed at 1600 r.p.m at a scan rate of  $5 \text{ mV}\cdot\text{s}^{-1}$  in a 0.1 M KOH solution. The catalyst ink was prepared by homogeneously mixing 5 mg of catalyst in a mixture of 0.95 mL of ethanol and 50  $\mu\text{L}$  of 5 wt% Nafion solution, followed by ultrasonication for several hours. The mass loading of MOF-NCNTs was  $0.708 \text{ mg}\cdot\text{cm}^{-2}$  on a glassy carbon (GC) disk electrode (3 mm in diameter). For comparative studies, the commercially available Pt/C (40 wt% Pt, JJ040, China) and  $\text{RuO}_2$  (99.9%, Macklin) were tested according to a similar procedure for the ORR and OER. The electron transfer number ( $n$ ) is calculated by the Koutecky-Levich equation at various electrode potentials:

$$\frac{1}{i} = \frac{1}{i_k} + \frac{1}{i_d} = \frac{1}{nFAkC_0} + \frac{1}{B\omega^{1/2}} \quad (3)$$

$$B = 0.62nFC_0D_0^{2/3}V^{-1/6} \quad (4)$$

where  $i$ ,  $i_k$  and  $i_d$  represent measured, kinetic, and diffusion-limiting current, respectively.  $F$  is the Faraday constant ( $96,485 \text{ C}\cdot\text{mol}^{-1}$ ).  $A$  is the geometric electrode area ( $0.07065 \text{ cm}^2$ );  $k$  is the rate constant for ORR ( $\text{m}\cdot\text{s}^{-1}$ );  $C_0$  is the saturated concentration of oxygen in 0.1 M KOH solution ( $1.2 \times 10^{-6} \text{ mol}\cdot\text{cm}^{-3}$ );  $D_0$  is the diffusion coefficient of oxygen in 0.1 M KOH solution ( $1.9 \times 10^{-5} \text{ cm}^2\cdot\text{s}^{-1}$ );  $V$  is the kinematic viscosity of solution ( $0.01 \text{ cm}^2\cdot\text{s}^{-1}$ ); and  $\omega$  is the angular rotation speed ( $\text{rad}\cdot\text{s}^{-1}$ ).

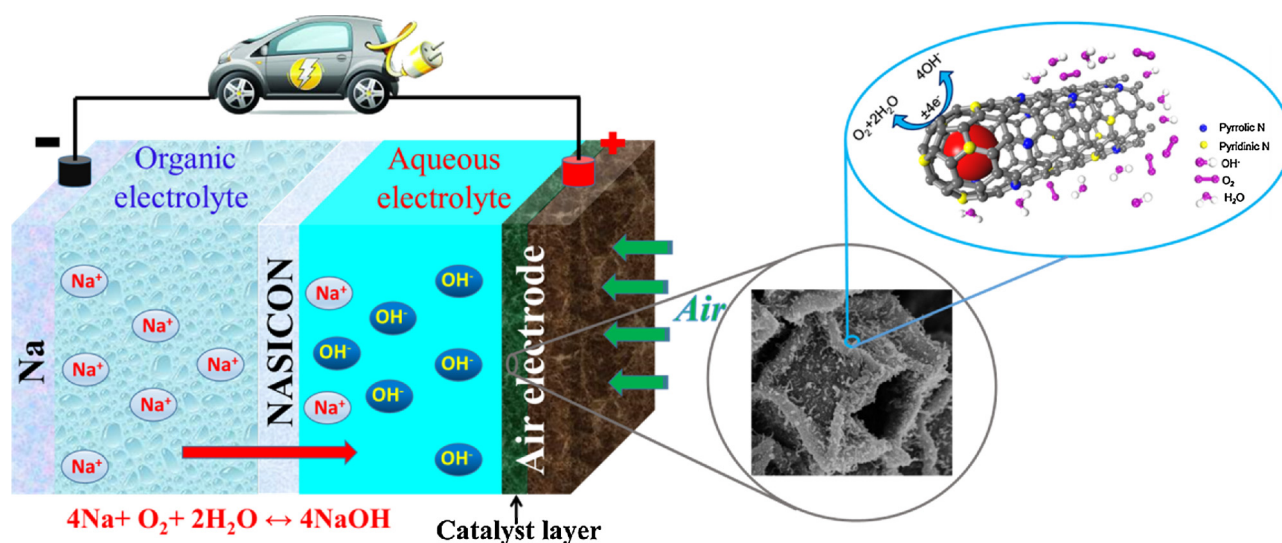


Fig. 1. Schematic illustration of a typical hybrid sodium-air battery and the ORR and OER process at the surface of Co confined in MOF-NCNTs.

#### 2.4. Hybrid SAB tests

The air-electrodes for hybrid SABs were prepared as follows. First, the gas diffusion layer (GDL) was obtained by a typical procedure [33]. Then, a slurry was made by dispersing 15 mg of the MOF-NCNT catalyst and 4 mg of conductive carbon powder in a solvent mixture of 1 mL ethanol and 1 mL deionized water, followed by one drop of 5% PTFE binder. Then, the slurry was homogeneously coated onto the GDL and the catalyst layer was pressed onto the nickel mesh for the fabrication of the air electrode. The mass loading of the MOF-NCNT catalyst was  $2 \text{ mg} \cdot \text{cm}^{-2}$ . For comparison, the 40 wt% Pt/C (JJ040, China), RuO<sub>2</sub> (99.9%, Macklin), Co-CNTs (Dongying technology, China), 3.46 wt% N-doped carbon nanotubes (NCNTs, DK nano, China), Multi-walled carbon nanotubes (MWNTs, DK nano, China)-coated GDL and uncoated carbon papers (EBORY, China) were prepared with the same mass loading.

The synthesized MOF-NCNT catalysts were used in hybrid SABs. Fig. 1 shows a schematic of the hybrid SAB applied in current research and the ORR and OER process at the surface of Co confined in the NCNTs. The Na<sub>3</sub>Zr<sub>2</sub>Si<sub>2</sub>PO<sub>12</sub> solid electrolyte (NASICON, ionic conductivity of  $1.3 \times 10^{-3} \text{ S} \cdot \text{cm}^{-1}$  at 25 °C) was used to separate the 1 M NaOH aqueous electrolyte and 1 M NaClO<sub>4</sub> in EC/DMC(1:1) with 1-vol % FEC organic electrolyte. We have demonstrated that the NASICON separator was immersed in the 1 M NaOH anode at room temperature for 20 days without significant change observed in the XRD pattern of the NASICON (Figure S1). The NASICON solid electrolyte is acceptably stable in the presence of the organic electrolyte and alkaline aqueous electrolyte [34,35]. The mechanism of hybrid SABs has been discussed in our previous work [1–4]. The electrochemical performances of the SABs were tested at 30 °C with a relative humidity (RH) of 70%. The charge and discharge behavior of the hybrid SABs were tested on a LAND battery testing station (CT2001 A, Wuhan LAND electronics).

### 3. Results and discussion

#### 3.1. Characterization of MOF-NCNTs

The crystallinity of the as-prepared MOF-NCNTs was characterized by XRD, shown in Fig. 2a. There are well-defined peaks at 44.2°, 51.5°, 75.8° corresponding to (111), (200), and (220) planes of the metallic cobalt nanoparticles (JCPDS No.15-0806), respectively. The peak at 26.2° corresponds to the carbon (002) plane, indicating the diffraction of graphitic structure [28]. The Raman spectrum of MOF-NCNTs also demonstrates the D band and G band corresponding to the defect/

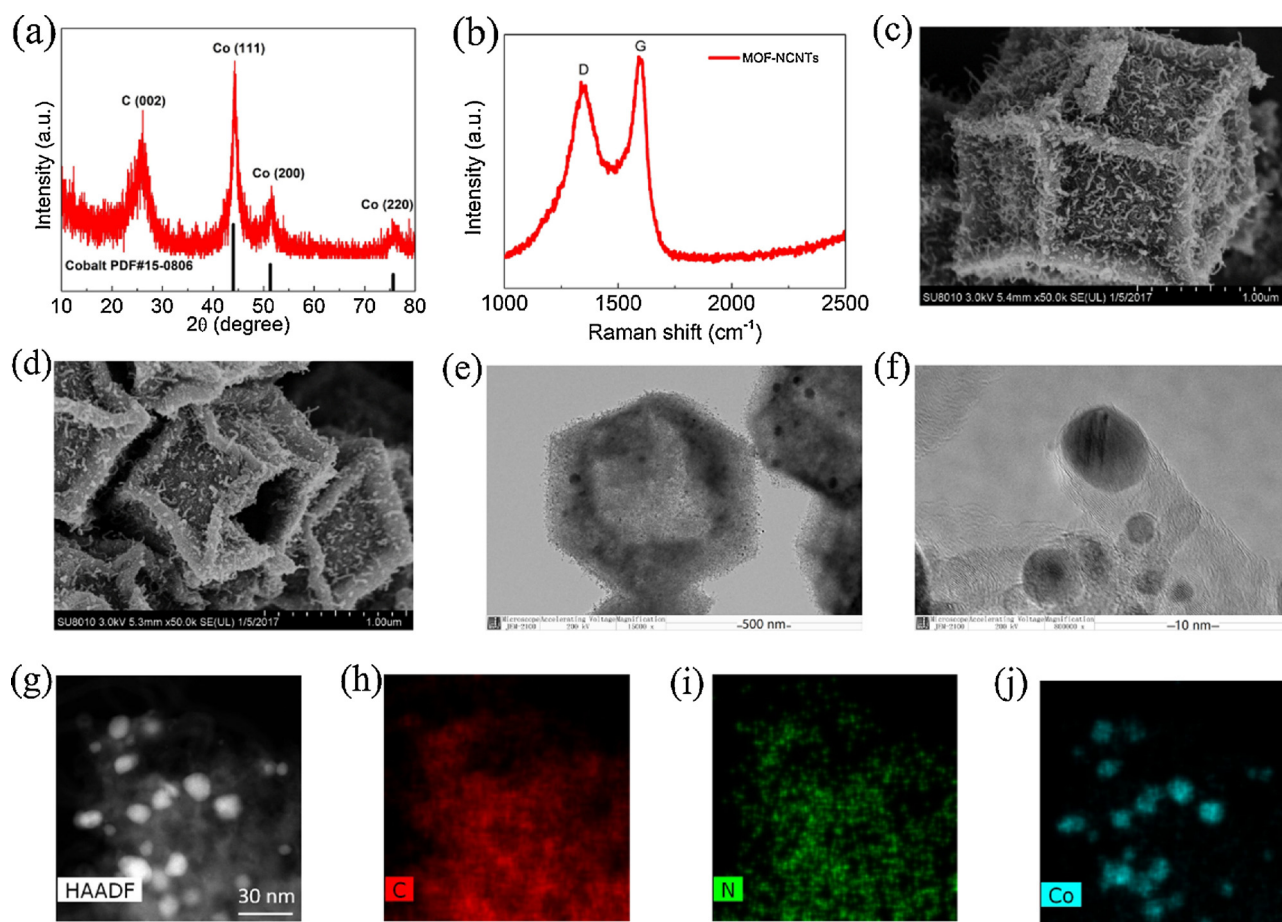
disordered carbon and graphitic carbon (Fig. 2b), respectively. It is reported that the carbon graphitization in the electrocatalysts can improve the electronic conductivity and corrosion resistance in electrocatalysis [36]. The defect/disordered carbon can provide catalytic active sites. The value of  $I_D/I_G$  (0.9) indicates a relatively high ratio of graphitic carbon and acceptable density of defect/disordered carbons, which contributes to the superior catalytic activity of the MOF-NCNTs.

Fig. 2c shows the FESEM images of the MOF-NCNTs obtained by heat-treating ZIF-67 particles at 700 °C in the presence of H<sub>2</sub>. The particles possess a polyhedral morphology and a rough surface, on which many CNTs are grown (Figure S2). The tiny network of crystalline CNTs not only enhances the efficiency of mass transport and superior corrosion resistance, but also improves electronic conductivity [37,38]. As shown in Fig. 2d, some particles reveal open pores, indicating the establishment of a porous cage structure. The interconnected CNTs grow on the hollow framework surface with a thickness about 200 nm. This is beneficial as it increases the specific surface area of the MOF-NCNTs to enhance mass transfer and electrolyte diffusion during electrochemical reactions [39].

The morphology and microstructure of the MOF-NCNTs were further characterized by TEM. Fig. 2e shows the particle length of the MOF-NCNT catalyst is in the range of 500–600 nm containing an open pore structure with a shell composed of CNTs. As shown in Fig. 2f, some cobalt nanoparticles are sealed by several layered graphitic carbon shells at the top of the CNTs. The interconnected CNTs grow on the hollow MOF surface in accordance with the results of HRTEM images (Figure S3a). The graphitic layers in the CNT walls are not completely parallel to the axis direction of the CNTs, resulting in plentiful graphitic edges exposed on the surface of CNTs, which are favorable for improving catalytic activity (Figure S3b).

To demonstrate the specific active sites of MOF-NCNTs, the HAADF-STEM was employed. As shown in Fig. 2g, a number of atomically dispersed bright spots are attributed to Co atoms by contrasting characteristic of atomic number. Fig. 2h–j shows C, N, and Co elemental mappings from EDS analysis, respectively. The nitrogen and cobalt atoms were evenly scattered amongst carbon, indicating successful N and Co dopant within the CNTs. In addition, figure S4 also showed the metal Co nanoparticle mainly distributed on the top of the CNTs. It can be suggested that with the growth of CNTs under the catalysis of Co nanoparticle and Co nanoparticle were simultaneously doped in the CNTs. The highly dispersed Co species and N dopants in the CNTs as active sites can improve the electrocatalysis performance of MOF-NCNTs. Open porous cage structures composed of N-doped carbon nanotubes are formed in the H<sub>2</sub> atmosphere during the thermal





**Fig. 2.** Representative (a) XRD; (b) Raman (c, d); FESEM; (e, f) TEM images of MOF-NCNTs; (g) HAADF-STEM image of MOF-NCNTs and the corresponding element mapping of (h) C, (i) N, and (j) Co.

treatment and it is clear that the open pore structure is formed before the acid leaching treatment (Figure S5) [40]. The open porous framework structure is derived from the ZIF-67 particles which provided the carbon and nitrogen source for the growth of MOF-NCNTs with the assistance of the catalytic metallic cobalt nanoparticles [32,40,41]. The carbon-sealed cobalt nanoparticles were retained during acid treatment due to the complete seal of the graphitic carbon shell.

In order to further investigate the evolution of MOF-NCNTs, the microstructure at different temperatures were observed. At a higher temperature of 750 °C, a greater density of longer CNTs are present on much rougher surface, indicating a more complete pyrolysis process but poor N dopants and low defect density (Figure. S6a) [32]. With a decrease in temperature to 650 °C, incomplete pyrolysis leads to the formation of shorter CNT clusters and some wrinkles (Figure. S6c). The structure formed at 700 °C is a robust open porous cage structure with NCNTs, which is most favorable for catalytic applications.

N<sub>2</sub> sorption isotherms of MOF-NCNTs are showed in Figure S7. The curve of MOF-NCNTs can be identified as type-IV isotherms with pronounced hysteresis loop, suggesting the formation of mesoporous structure (Figure S7). Moreover, the MOF-NCNTs material exhibits a relatively broad mesoporous distribution, with an average pore size of ~11.4 nm according to the density functional theory model (DFT) (inset of Fig. S7). The specific surface area estimated by the Brunauer-Emmett-Teller (BET) method and the total pore volume are 446 m<sup>2</sup> g<sup>-1</sup> and 1.27 cm<sup>3</sup> g<sup>-1</sup>, respectively.

In order to investigate the catalytic properties of MOF-NCNTs, XPS was used to characterize the chemical composition and the effect of nitrogen doping for MOF-NCNTs. As shown in Fig. 3a, the full XPS spectrum revealed that the as-obtained MOF-NCNTs consist of Co, C, N,

O with a nitrogen content of around 1.30%. As can be observed from Fig. 3b, the N 1s spectrum was deconvoluted into three types of nitrogen peaks, corresponding to typical pyridinic N at 398.6 eV, Co-N<sub>x</sub> at 399.9 eV and graphitic N at 401.0 eV [42]. The pyridinic N atoms play an important role in the excellent electrocatalytic activity for ORR/OER process due to the strong electronic affinity, which is beneficial for the adsorption of oxygen atoms and electronic interactions [43–46]. The N-containing species of the Co-N<sub>x</sub> and graphitic N were demonstrated to be favorable for the onset potential and the limiting current density, respectively, resulting in the outstanding ORR catalytic activity [42]. The Co 2p<sub>3/2</sub> spectrum showed the presence the two types of cobalt bands, Co-N<sub>x</sub> at 780.3 eV and Co-Co at 778.7 eV [47].

### 3.2. Electrocatalyst performances of MOF-NCNTs and application

To further demonstrate the ORR catalytic activity of MOF-NCNTs, linear scan voltammetry (LSV) measurements were performed using a rotating disk electrode at various rotations rates under an O<sub>2</sub>-saturated 0.1 M KOH solution (Figure S8a). Based on the LSV curve at various rotation rates, the Koutecky-Levich equation and the linearity of the K-L plot is used to investigate the electron transfer number (n) at different potentials (Figure S8b). The value of n is calculated to be 3.70–3.92 at the potential of 0.55–0.75 V, suggesting a 4 electron ORR pathway. As shown in Fig. 4a, the good ORR catalytic activity of MOF-NCNTs was reflected by a relatively higher onset potential than the commercial Pt/C. The half-wave potential of MOF-NCNTs is 9 mV higher than the commercial Pt/C catalyst (E<sub>1/2</sub>: 0.850 V versus 0.841 V), suggesting the excellent ORR activity is a result of the MOF-NCNTs catalyst. Moreover, the MOF-NCNTs displayed the most

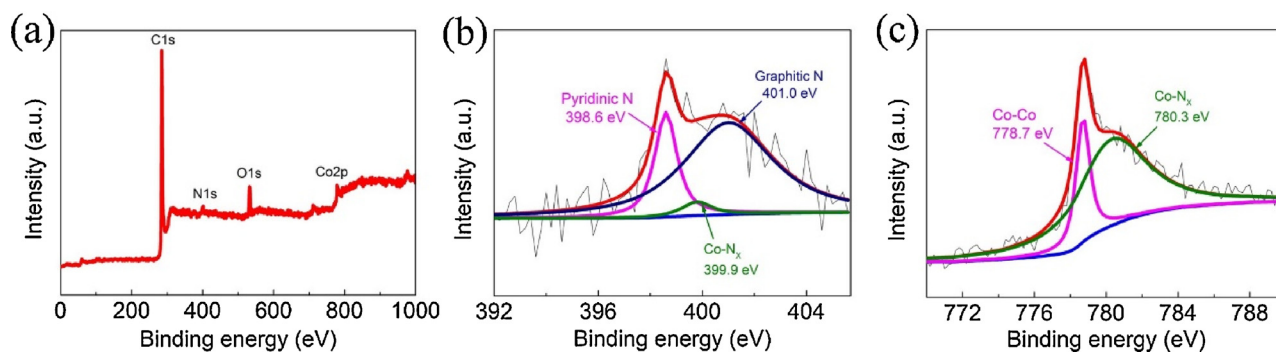


Fig. 3. (a) XPS survey spectra and high-resolution spectra of (b) N 1s and (c) Co 2p<sub>3/2</sub> of MOF-NCNTs.

excellent catalytic activity for ORR compared to that of the MOFs obtained at 650 °C and 750 °C. As shown in Fig. 4b, the OER polarization curves of the all MOFs samples, Pt/C and RuO<sub>2</sub> catalyst were investigated in an N<sub>2</sub> saturated 0.1 M KOH solution at 1600 r.p.m. The MOF-NCNTs obtained at 700 °C exhibits the best OER activity compared with other temperatures prepared material. Moreover, the MOF-NCNTs exhibited a relatively lower onset potential compared to the commercial Pt/C catalyst, indicating superior OER activity of MOF-NCNTs. The MOF-NCNT catalyst showed a lower potential than Pt/C at a current density of 10 mA·cm<sup>-2</sup> versus reversible hydrogen electrode (RHE) (1.68 versus 1.78 V). Although the OER started at a slightly higher potential, the MOF-NCNTs showed similar potential to those of the RuO<sub>2</sub> at 10 mA·cm<sup>-2</sup> (1.68 versus 1.63 V, RHE). These results

demonstrated that the MOF-NCNT catalyst is an excellent bifunctional electrocatalyst for ORR and OER.

The MOF-NCNTs were used as the electrocatalyst for hybrid SABs, and the electrochemical performance of the batteries were investigated by galvanostatic charge-discharge processes at a current density of 0.1 mA·cm<sup>-2</sup>. As shown in Fig. 4c, the battery using the MOF-NCNT catalyst showed the best electrochemical behavior, exhibiting a high and stable discharge voltage of 2.80 V and round trip efficiency of 90.0%. In contrast, the commercial Pt/C (40 wt%), RuO<sub>2</sub> and carbon paper catalysts exhibited a discharge voltage of 2.76 V, 2.64 V and 2.20 V with corresponding round trip efficiencies of 85%, 84% and 65%, respectively. Compared with the Pt/C and RuO<sub>2</sub> catalyst, the batteries using the MOF-NCNT catalyst displayed higher discharge

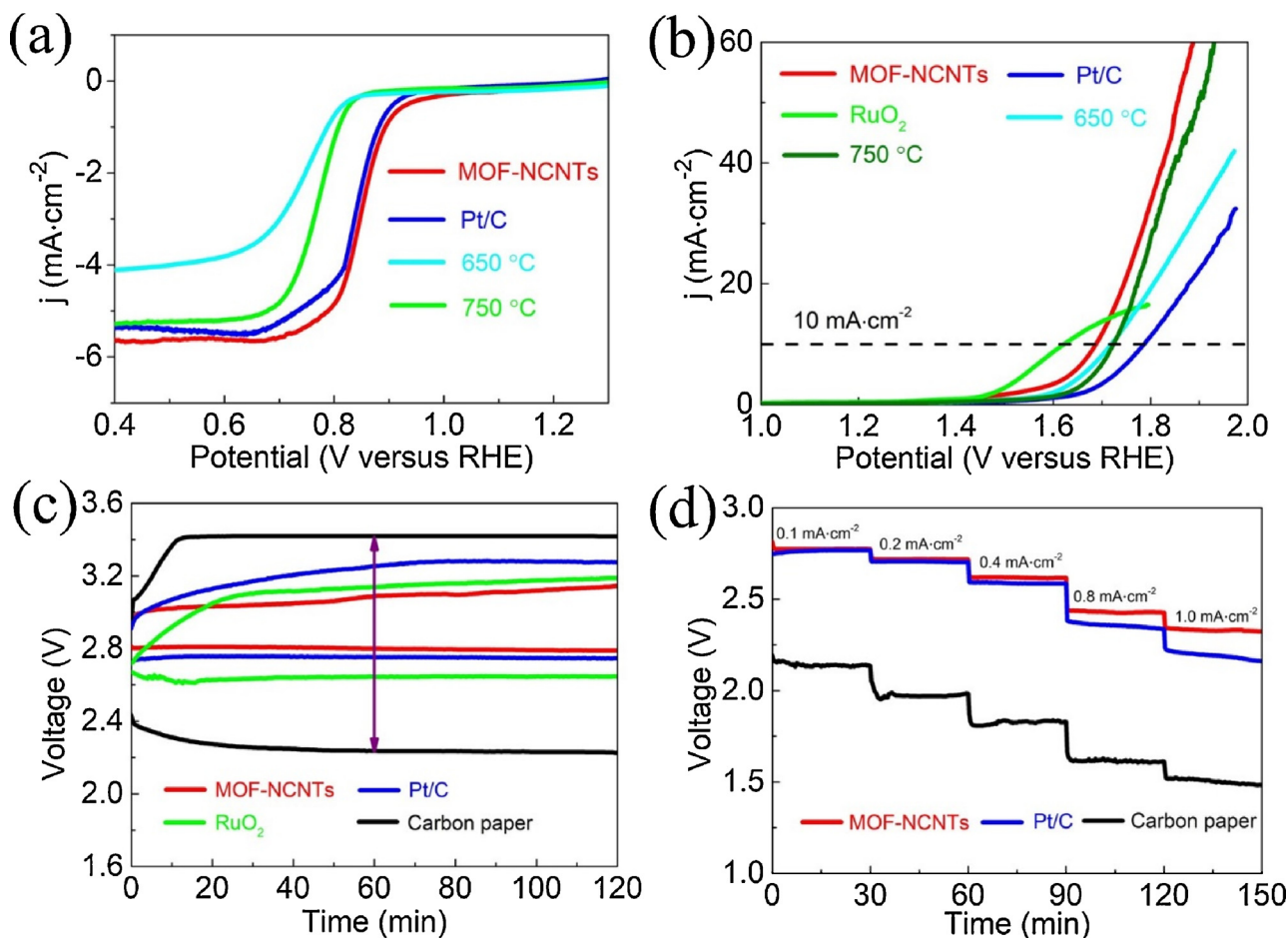


Fig. 4. (a) ORR and (b) OER polarization curves of all MOFs samples, Pt/C, and RuO<sub>2</sub> catalysts in 0.1 M KOH solution; (c) Charge-discharge curves of hybrid sodium-air batteries using MOF-NCNTs, Pt/C, RuO<sub>2</sub>, and carbon paper catalysts at a current density of 0.1 mA·cm<sup>-2</sup>; (d) Discharge voltage curves of hybrid sodium-air batteries using different catalysts at different current densities.

**Table 1**  
Discharge–charge performance of hybrid sodium-air batteries with different catalysts.

Catalysts	Discharge voltage (V, plateau)	Charge voltage (V, plateau)	Voltage gap <sup>a</sup> (V)	Current densities/NaOH concentration (mol·L <sup>-1</sup> )	Ref.
<i>dp</i> -MnCo <sub>2</sub> O <sub>4</sub> /N-rGO	2.75	3.14	0.39	0.13 mA·cm <sup>-2</sup> /1	[3]
Mn <sub>3</sub> O <sub>4</sub> /C	2.60	3.51	0.91	1 mA·cm <sup>-2</sup> /1	[4]
Carambola-shaped VO <sub>2</sub>	2.81	3.45	0.64	0.01 mA·cm <sup>-2</sup> /0.1	[6]
Pt/C <sup>1</sup>	2.94	3.55	0.61	0.01 mA·cm <sup>-2</sup> /0.1	[6]
Pt/C <sup>2</sup>	2.85	3.38	0.53	0.025 mA·cm <sup>-2</sup> /0.1	[16]
GNS/MC	2.98	3.10	0.12	60 mA g <sup>-1</sup> /0.1	[20]
Pt/C <sup>3</sup>	3.03	3.21	0.18	60 mA g <sup>-1</sup> /0.1	[20]
Co <sub>3</sub> (PO <sub>4</sub> ) <sub>2</sub>	2.82	3.41	0.59	0.01 mA·cm <sup>-2</sup> /0.1	[48]
MOF-NCNTs	2.80	3.10	0.30	0.1 mA·cm <sup>-2</sup> /1	Present work
Pt/C	2.76	3.26	0.50	0.1 mA·cm <sup>-2</sup> /1	Present work
NCNTs	2.64	3.41	0.77	0.1 mA·cm <sup>-2</sup> /1	Present work
MWNTs	2.51	3.41	0.90	0.1 mA·cm <sup>-2</sup> /1	Present work
Co-CNTs	2.74	3.41	0.67	0.1 mA·cm <sup>-2</sup> /1	Present work
RuO <sub>2</sub>	2.64	3.14	0.50	0.1 mA·cm <sup>-2</sup> /1	Present work
MOFs-650 °C	2.67	3.21	0.64	0.1 mA·cm <sup>-2</sup> /1	Present work
MOFs-750 °C	2.68	3.19	0.61	0.1 mA·cm <sup>-2</sup> /1	Present work
Carbon paper	2.22	3.40	1.18	0.1 mA·cm <sup>-2</sup> /1	Present work

<sup>a</sup> Voltage gap calculation based on charge–discharge voltage plateau. Pt/C<sup>1</sup>, Pt/C<sup>2</sup>, and Pt/C<sup>3</sup> represent batteries tested under different current density and NaOH concentrations.

plateau and lower charge plateau, suggesting superior ORR and OER catalytic performance of MOF-NCNT. Most importantly, the batteries using the MOF-NCNT catalyst displayed the most narrow voltage gap of 0.30 V compared to that of Pt/C (0.50 V), RuO<sub>2</sub> (0.50 V), Co-CNTs (0.67 V), NCNTs (0.77 V), MWNTs (0.90 V), 650 °C (0.64 V), 750 °C (0.61 V), and carbon paper (1.18 V) (Table 1, Figure S8c).

As we can see from Fig. 4d, the discharge voltage of MOF-NCNTs is the highest compared to Pt/C and carbon paper at different current densities. Increasing the current density from 0.1 mA·cm<sup>-2</sup> to 1.0 mA·cm<sup>-2</sup> during the discharge process results in a voltage drop of 0.44 V, 0.57 V and 0.63 V for MOF-NCNTs, Pt/C and carbon paper,

respectively, indicating that the MOF-NCNTs have superior catalytic activity and stability. Additionally, the discharge voltage decreases almost linearly with increasing the current density (Figure S8d) and the fitted slopes of the catalysts are in accordance with the trend of MOF-NCNTs < Pt/C < carbon paper, demonstrating the excellent catalytic performance of the MOF-NCNTs compared with Pt/C and carbon paper.

The cycling performance of the hybrid SABs with MOF-NCNT catalysts were measured at 0.1 mA·cm<sup>-2</sup> for 35 cycles. As can be seen from Fig. 5a, the voltage gap at the first cycle was approximately 0.30 V, indicating exceptional electrocatalytic activity of MOF-NCNTs. The average discharge plateau is 2.81 V, resulting in a high round trip efficiency of 87% over 35 cycles. Meanwhile, the FESEM image of the catalyst structure is observed, which showed the identical polyhedron morphology and structure of MOF-NCNTs before (Fig. 5b) and after (Fig. 5c) cycling, implying the excellent stability of MOF-NCNTs. However, the charge voltage increases from 3.12 to 3.30 V over 35 cycles, which could be attributed to the increased NaOH concentration by evaporating of water in aqueous electrolyte, resulting in a slight decline to electrochemical performance of hybrid SABs [1,4]. However, when a small amount of water was re-introduced into the aqueous electrolyte, the SAB system once again demonstrates good cycling performance (Figure S9).

The excellent catalytic activity and stability of MOF-NCNTs was demonstrated by the lack of change in the catalyst structure as shown in the FESEM images before and after cycling. In addition, the electrochemical performance can be further stabilized by reintroducing fresh aqueous electrolyte to the hybrid SABs. In the future, this issue can be resolved by employing a peristaltic pump to maintain a constant concentration of NaOH to enhance the electrochemical performance of hybrid SABs [1,49].

### 3.3. The role of MOF and NCNT

The superior electrochemical behavior of MOF-NCNTs can mainly be ascribed to the synergistic effect between N dopants and confined Co nanoparticles within the CNT, the structure of the NCNTs formed, and their robust open porous framework structure [32,47,50]. In previous reports, the work functions and densities of states (DOS) of carbon-based electrocatalysts were used as effective parameters for demonstrating the ORR activity [51,52]. Meng et al. demonstrated the synergistic effect between N dopants and confined Co particles in CNTs increases the densities of states (DOS) near the Fermi level and reduces the work function by density functional theory (DFT) simulations, hence improving the ORR catalytic performance [47]. The electronegative N dopants induce a higher positive charge density on adjacent carbon atoms, which is beneficial for the adsorption and reduction of oxygen atoms in the NCNTs, resulting in excellent ORR/OER catalytic activity of MOF-NCNTs [27,53–55]. The structure of NCNTs also improved the gas and liquid transport, electronic conductivity, as well as corrosion resistance [11,37]. Moreover, the metallic Co nanoparticles sealed by the graphitic carbon shell greatly improve catalytic activity due to the electronic interaction between metal nanoparticles and NCNTs shell, thereby accelerating the formation of the OOH species [56]. Interaction between cobalt nanoparticles and NCNTs affected the properties of the outer walls, which induced more O<sub>2</sub> adsorption active sites [47,57–59]. The robust porous framework structure improved electrocatalytic stability and activity by promoting mass transport, and electronic interactions during the ORR and OER process [31,60,61].

In addition, the Co-CNT and N-CNT display a higher discharge voltage than MWNT due to the Co dopants or electronegative N dopants [11,31]. Compared with NCNTs and MWNTs, Co-CNTs exhibited a relatively higher discharge voltage, suggesting the contribution of metal Co nanoparticle for ORR catalytic performance. Moreover, the work function value of Co4@CNTs (3.92 eV) is smaller than pure CNTs (4.2 eV) from DFT simulations. This reduced work function is expected to enhance its chemical activity [47]. Nevertheless, the N-CNT or Co-CNT show unsatisfactory ORR and OER catalytic performance compared to MOF-NCNT because of the reduced number of active sites. Furthermore, as compared with other catalysts in previous reports (Table 1), the MOF-NCNTs exhibited superior ORR and OER activity under the same conditions due to the synergistic effect of N and Co inducing more catalytic active sites [37,62]. Moreover, the three-



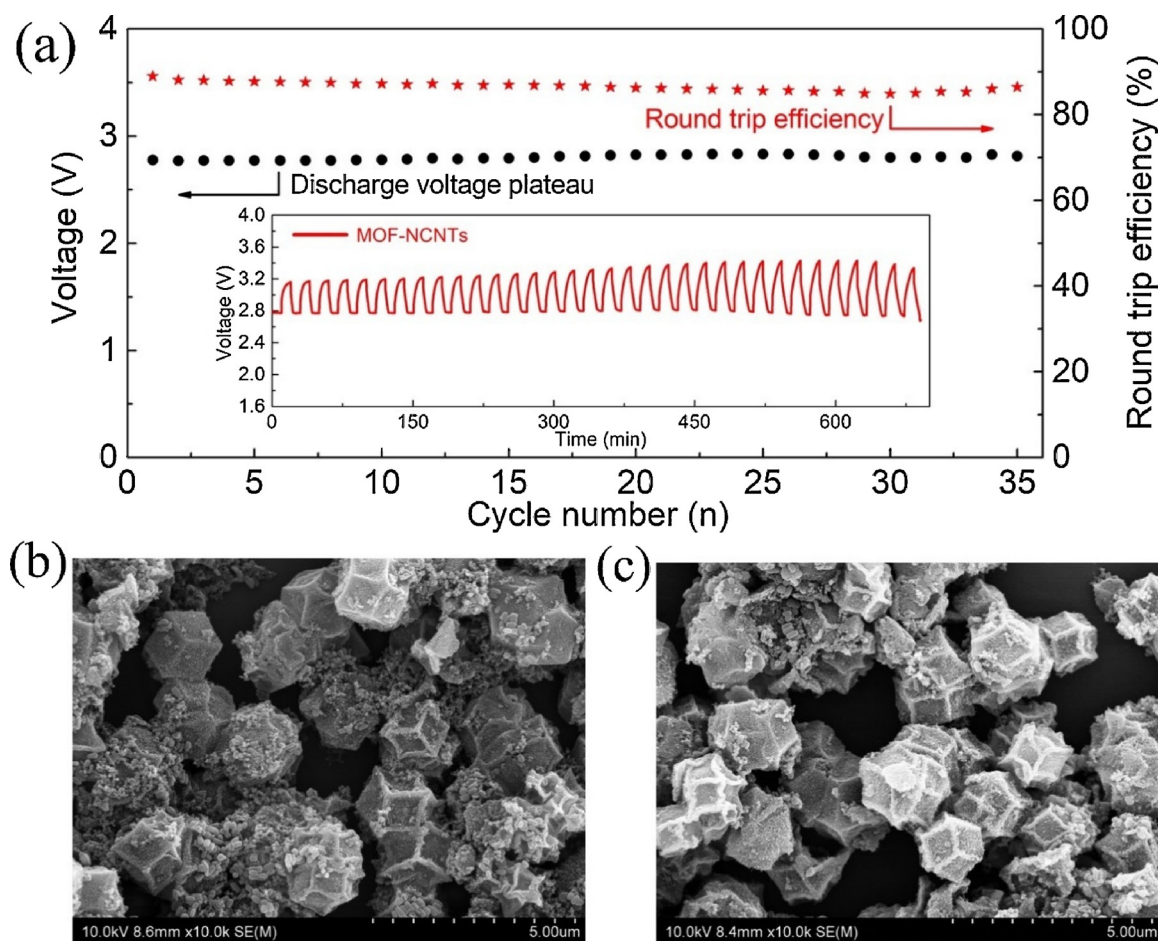


Fig. 5. (a) Cycling performance of hybrid sodium-air batteries with MOF-NCNTs as catalyst at  $0.1 \text{ mA}\cdot\text{cm}^{-2}$  for 35 cycles. FESEM images of the catalyst structure before (b) and after (c) cycling.

dimensional hierarchical porous structure and carbon nanotubes of MOF-NCNTs provide a large specific area, which enhances electrocatalytic activity by promoting mass transport and electronic interactions during the electrochemical reaction [31,60,61].

#### 4. Conclusions

MOF-NCNT catalysts were synthesized for hybrid SABs using ZIF-67 particles as the precursor. By calcinating in  $\text{Ar}/\text{H}_2$  atmosphere at  $700^\circ\text{C}$ , the ZIF-67 precursor was pyrolyzed and converted into hierarchical shells of interconnected crystalline NCNTs with a robust hollow framework structure. The MOF-NCNTs demonstrated efficient and stable bifunctional electrocatalyst performance for the ORR and OER within hybrid SABs. Compared with commercial Pt/C and  $\text{RuO}_2$ , MOF-NCNT demonstrated remarkable electrocatalytic activity and stability. A low voltage gap of  $0.30 \text{ V}$  was obtained at a current density of  $0.1 \text{ mA}\cdot\text{cm}^{-2}$ , resulting in a high round trip efficiency of 90% for the first cycle. In addition, hybrid SABs showed good cycling performance with an average discharge voltage of  $2.81 \text{ V}$ , resulting in a high round trip efficiency of 87% after 35 cycles. This behavior can be ascribed to nitrogen-doped sites and confined Co nanoparticles within the CNTs, which induces more sites for oxygen adsorption and electron transfer. The robust open porous framework structure consisting of interconnected NCNTs enhanced the electrocatalytic activity and stability of MOF-NCNTs. This study provides a new avenue for developing cathode electrocatalysts and demonstrates the promising application of MOF-derived catalysts in metal-air battery systems.

#### Acknowledgements

This work was financially supported by the National Natural Science Foundation of China (51704136, 11765010), the Applied Basic Research Programs of Yunnan Provincial Science and Technology Department (2016FB087), the project of Academician free exploration project of Yunnan Province (2018HA006), the Program for Innovative Research Team in University of Ministry of Education of China (IRT17R48). This research was supported by Natural Sciences and Engineering Research Council of Canada, Canada Research Chair Program, and the University of Western Ontario.

#### Appendix A. Supplementary data

Supplementary material related to this article can be found, in the online version, at doi:<https://doi.org/10.1016/j.apcatb.2018.09.063>.

#### References

- [1] Y. Kang, F. Liang, K. Hayashi, *Electrochim. Acta* 218 (2016) 119–124.
- [2] K. Hayashi, K. Shima, F. Sugiyama, *J. Electrochem. Soc.* 160 (2013) A1467–A1472.
- [3] Y. Kang, D. Zou, J. Zhang, F. Liang, K. Hayashi, H. Wang, D. Xue, K. Chen, K.R. Adair, X. Sun, *Electrochim. Acta* 244 (2017) 222–229.
- [4] F. Liang, K. Hayashi, *J. Electrochem. Soc.* 162 (2015) A1215–A1219.
- [5] S.M. Hwang, W.S. Go, H. Yu, Y. Kim, *J. Mater. Chem. A* 5 (2017) 11592–11600.
- [6] Z. Khan, B. Senthilkumar, S.O. Park, S. Park, J. Yang, J.H. Lee, H.K. Song, Y. Kim, S.K. Kwak, H. Ko, *J. Mater. Chem. A* 5 (2017) 2037–2044.
- [7] P. Hartmann, C.L. Bender, M. Vracar, A.K. Durr, A. Garsuch, J. Janek, P. Adelhelm, *Nat. Mater.* 12 (2013) 228–232.
- [8] T. Hashimoto, K. Hayashi, *Electrochim. Acta* 182 (2015) 809–814.
- [9] W.M. Liu, W.W. Yin, F. Ding, L. Sang, Z.W. Fu, *Electrochem. Commun.* 45 (2014)

- 87–89.
- [10] R.B. Araujo, S. Chakraborty, R. Ahuja, *Phys. Chem. Chem. Phys.* 17 (2015) 8203–8209.
  - [11] H. Yadegari, M.N. Banis, B.W. Xiao, Q. Sun, X. Li, A. Lushington, B.Q. Wang, R.Y. Li, T.K. Sham, X.Y. Cui, X.L. Sun, *Chem. Mater.* 27 (2015) 3040.
  - [12] H. Yadegari, Q. Sun, X. Sun, *Adv. Mater.* 28 (2016) 7065–7093.
  - [13] H. Yadegari, M. Banis, A. Lushington, Q. Sun, R. Li, T.-K. Sham, X. Sun, *Energy Environ. Sci.* 10 (2017) 286–295.
  - [14] J. Lu, L. Li, J.B. Park, Y.K. Sun, F. Wu, K. Amine, *Chem. Rev.* 114 (2014) 5611–5640.
  - [15] M.H. Cho, J. Trottier, C. Gagnon, P. Hovington, D. Clément, A. Vijh, C.S. Kim, A. Guerfi, R. Black, L. Nazar, K. Zaghib, *J. Power Sources* 268 (2014) 565–574.
  - [16] S. Sahgong, S.T. SenthilKumar, K. Kim, S.M. Hwang, Y. Kim, *Electrochem. Commun.* 61 (2015) 53–56.
  - [17] F. Liang, T. Watanabe, K. Hayashi, Y. Yao, W. Ma, Y. Bin, Y. Dai, *Mater. Lett.* 187 (2017) 32–35.
  - [18] A. Arul, H. Pak, K.U. Moon, M. Christy, M.Y. Oh, K.S. Nahm, *Appl. Catal. B-Environ.* 220 (2018) 488–496.
  - [19] S. Dong, X. Chen, S. Wang, L. Gu, L. Zhang, X. Wang, X. Zhou, Z. Liu, P. Han, Y. Duan, H. Xu, J. Yao, C. Zhang, K. Zhang, G. Cui, L. Chen, *ChemSusChem* 5 (2012) 1712–1715.
  - [20] J.Y. Cheon, K. Kim, Y.J. Sa, S.H. Sahgong, Y. Hong, J. Woo, S.D. Yim, H.Y. Jeong, Y. Kim, S.H. Joo, *Adv. Energy Mater.* (2016) 1501794.
  - [21] M. Abirami, S.M. Hwang, J. Yang, S.T. SenthilKumar, J. Kim, W.S. Go, B. SenthilKumar, H.K. Song, Y. Kim, *ACS Appl. Mater. Interfaces* 8 (2016) 32778–32787.
  - [22] M. Alhamami, H. Doan, C.H. Cheng, *Materials* 7 (2014) 3198–3250.
  - [23] H. Furukawa, K.E. Cordova, M. O’Keeffe, O.M. Yaghi, *Science* 341 (2013) 1230444.
  - [24] Y. Zhao, Z. Song, X. Li, Q. Sun, N. Cheng, S. Lawes, X. Sun, *Energy Storage Mater.* 2 (2016) 35.
  - [25] J. Qiu, X. Zhang, Y. Feng, X. Zhang, H. Wang, J. Yao, *Appl. Catal. B-Environ.* 231 (2018) 317–342.
  - [26] J. Ying, J. Li, G. Jiang, Z.P. Cano, Z. Ma, C. Zhong, D. Su, Z. Chen, *Appl. Catal. B-Environ.* 225 (2018) 496–503.
  - [27] Z. Song, W. Liu, N. Cheng, M. Norouzi Banis, X. Li, Q. Sun, B. Xiao, Y. Liu, A. Lushington, R. Li, L. Liu, X. Sun, *Mater. Horiz.* 4 (2017) 900–907.
  - [28] P. Su, H. Xiao, J. Zhao, Y. Yao, Z. Shao, C. Li, Q. Yang, *Chem. Sci.* 4 (2013) 2941.
  - [29] R. Mi, H. Liu, H. Wang, K.-W. Wong, J. Mei, Y. Chen, W.-M. Lau, H. Yan, *Carbon* 67 (2014) 744–752.
  - [30] X. Lin, X. Lu, T. Huang, Z. Liu, A. Yu, *J. Power Sources* 242 (2013) 855–859.
  - [31] Q. Sun, H. Yadegari, M.N. Banis, J. Liu, B.W. Xiao, B.Q. Wang, S. Lawes, X. Li, R.Y. Li, X.L. Sun, *Nano Energy* 12 (2015) 698–708.
  - [32] B.Y. Xia, Y. Yan, N. Li, H.B. Wu, X.W. Lou, X. Wang, *Nat Energy* 1 (2016) 15006.
  - [33] Z. Xiong, S.J. Liao, D. Dang, X.L. Tian, S.Y. Hou, F.F. Liu, H.L. Peng, Z.Y. Fu, *J. Hydrogen Energy* 40 (2015) 3961–3967.
  - [34] F. Liang, X. Qiu, Q. Zhang, Y. Kang, A. Koo, K. Hayashi, et al., *Nano Energy* 49 (2018) 574–579.
  - [35] Y. Kang, F. Su, Q. Zhang, F. Liang, K.R. Adair, K. Chen, et al., *ACS Appl. Mater. Interfaces* 10 (2018) 23748–23756.
  - [36] Q. Zhu, W. Xia, T. Akita, R. Akita Akita, Q. Xu, *Adv. Mater.* 28 (2016) 6391–6398.
  - [37] G. Wu, A. Santandreu, W. Kellogg, S. Gupta, O. Ogoke, H. Zhang, H.L. Wang, L. Dai, *Nano Energy* 29 (2016) 83–110.
  - [38] P. Zhang, F. Sun, Z. Xiang, Z. Shen, J. Yun, D. Cao, *Energy Environ. Sci.* 7 (2014) 442–450.
  - [39] Y. Zhao, R. Nakamura, K. Kamiya, S. Nakanishi, K. Hashimoto, *Nat. Commun.* 4 (2013) 2390.
  - [40] J.K. Sun, Q. Xu, *Energy Environ. Sci.* 7 (2014) 2071.
  - [41] M. Hu, J. Reboul, S. Furukawa, N.L. Torad, Q. Ji, P. Srinivasu, K. Ariga, S. Kitagawa, Y. Yamauchi, *J. Am. Chem. Soc.* 134 (2012) 2864–2867.
  - [42] J. Song, Y. Ren, J. Li, X. Huang, F. Cheng, Y. Tang, H. Wang, *Carbon* (2018).
  - [43] Z.S. Wu, L. Chen, J. Liu, K. Parvez, H. Liang, J. Shu, H. Sachdev, R. Graf, X. Feng, K. Mullen, *Adv. Mater.* 26 (2014) 1450–1455.
  - [44] X. Zou, X. Huang, A. Goswami, R. Silva, B.R. Sathe, E. Mikmekova, T. Asefa, *Angew. Chem. Int. Ed.* 53 (2014) 4372–4376.
  - [45] Y. Hou, Z. Wen, S. Cui, S. Ci, S. Mao, J. Chen, *Adv. Funct. Mater.* 25 (2015) 872–882.
  - [46] Z.W. Seh, J. Kibsgaard, C.F. Dickens, I. Chorkendorff, J.K. Nørskov, T.F. Jaramillo, *Science* (2017) 355.
  - [47] J. Meng, C. Niu, L. Xu, J. Li, X. Liu, X. Wang, Y. Wu, X. Xu, W. Chen, Q. Li, Z. Zhu, D. Zhao, L. Mai, *J. Am. Chem. Soc.* 139 (2017) 8212–8221.
  - [48] B. SenthilKumar, Z. Khan, S. Park, I. Seo, H. Ko, Y. Kim, *J. Power Sources* 311 (2016) 29–34.
  - [49] H.T. Chung, W. J.H. Won, P. Zelenay, *Nat. Commun.* 4 (2013) 1922.
  - [50] R.V. Jagadeesh, K. Murugesan, A.S. Alshammari, H. Neumann, M.M. Pohl, J. Radnik, M. Beller, *Science* (2017) 358.
  - [51] J.Y. Cheon, J.H. Kim, J.H. Kim, K.C. Goddeti, J.K. Park, S.H. Joo, *J. Am. Chem. Soc.* 136 (2014) 8875–8878.
  - [52] D. Guo, R. Shibuya, C. Akiba, S. Saji, T. Kondo, J. Nakamura, *Science* 351 (2016) 361–365.
  - [53] K. Gong, F. Du, Z. Xia, M. Durstock, L. Dai, *Science* 323 (2009) 760–764.
  - [54] J. Shui, M. Wang, F. Du, L. Dai, *Sci. Adv.* 1 (2015) e1400129.
  - [55] S. Chen, J. Duan, J. Ran, M. Jaroniec, S.Z. Qiao, *Energy Environ. Sci.* 6 (2013) 3693–3699.
  - [56] D. Deng, L. Yu, X. Chen, G. Wang, L. Jin, X. Pan, J. Deng, G. Sun, X. Bao, *Angew. Chem. Int. Ed.* 52 (2013) 371–375.
  - [57] L. Wang, A. Ambrosi, M. Pumera, *Angew. Chem. Int. Ed.* 52 (2013) 13818–13821.
  - [58] G. Wu, K.L. More, C.M. Johnston, P. Zelenay, *Science* 332 (2011) 443–447.
  - [59] D. Deng, L. Yu, X. Chen, G. Wang, L. Jin, X. Pan, J. Deng, G. Sun, X. Bao, *Angew. Chem. Int. Ed.* 52 (2013) 371–375.
  - [60] W. Xiong, F. Du, Y. Liu, J. Albert Perez, M. Supp, T.S. Ramakrishnan, L. Dai, L. Jiang, *J. Am. Chem. Soc.* 132 (2010) 15839–15841.
  - [61] H.W. Liang, X. Zhuang, S. Brüller, X. Feng, K. Mullen, *Nat. Commun.* 5 (2014) 4973.
  - [62] S. Cai, Z. Meng, H. Tang, Y. Wang, P. Tsiakaras, *Appl. Catal. B-Environ.* 217 (2017) 477–484.